Dalton Transactions

ROYAL SOCIETY OF CHEMISTRY

PAPER

View Article Online
View Journal | View Issue

Cite this: *Dalton Trans.*, 2021, **50**, 14820

Al_2O_3 co-doped with Cr^{3+} and Mn^{4+}, a dual-emitter probe for multimodal non-contact luminescence thermometry

V. B. Mykhaylyk, *[a] H. Kraus,[b] L.-I. Bulyk,[c] I. Lutsyuk,[d] V. Hreb,[d] L. Vasylechko,[d] Y. Zhydachevskyy,[c,d] A. Wagner[a] and A. Suchocki[c]

Luminescence probes that facilitate multimodal non-contact measurements of temperature are of particular interest due to the possibility of cross-referencing results across different readout techniques. This intrinsic referencing is an essential addition that enhances accuracy and reliability of the technique. A further enhancement of sensor performance can be achieved by using two luminescent ions acting as independent emitters, thereby adding in-built redundancy to non-contact temperature sensing, using a single readout technique. In this study we combine both approaches by engineering a material with two luminescent ions that can be independently probed through different readout modes of non-contact temperature sensing. The approach was tested using Al_2O_3 co-doped with Cr^{3+} and Mn^{4+}, exhibiting sharp emission lines due to $^2E \rightarrow {}^4A_2$ transitions. The temperature sensing performance was examined by measuring three characteristics: temperature-induced changes of the intensity ratio of the emission lines, their spectral position, and the luminescence decay time constant. The processes responsible for the changes with temperature of the measured luminescence characteristics are discussed in terms of relevant models. By comparing temperature resolutions achievable by different modes of temperature sensing it is established that in Al_2O_3-Cr,Mn spectroscopic methods provide the best measurement accuracy over a broad temperature range. A temperature resolution better than ±2.8 K can be achieved by monitoring the luminescence intensity ratio (40–145 K) and the spectral shift of the R-line of Mn^{4+} (145–300 K range).

Received 24th August 2021,
Accepted 23rd September 2021

DOI: 10.1039/d1dt02836g

rsc.li/dalton

1. Introduction

When reliable temperature measurements are required in challenging applications, such as in harsh environments or with restricted access to an object of interest, non-contact probes with all their advantages are the temperature sensors of choice.[1–3] Examples include very hot or cold apparatus, aggressive chemicals, and strong electromagnetic and radiation fields where the necessity of isolation, shielding, or motion of the object would add complications. Many areas of science and technology benefit from using this method, such as aerospace,[4] catalysis,[5] life science,[6] medicine[7] and biology.[8,9] Importantly, it is one of the few methods capable of delivering temperature mapping with submicron spatial resolution.[10,11] Thus, the field of luminescence thermometry develops rapidly, as demonstrated by a steady stream of publications and reviews.[12–17]

Temperature changes affect a range of luminescence characteristics, such as shapes of emission spectra, intensities, or luminescence decay time constants. Either of these observables can be used to monitor temperature.[16,18] The choice of detection scheme is often governed by the sensitivity to temperature changes that a sensor's specific luminescence characteristics exhibits. Most common are luminescence decay time and intensity ratio of two peaks.[14] The intensity ratio method compares the emission intensities observed from two thermally coupled levels, obeying Boltzmann statistics. The energy difference between the two levels defines the range of temperatures where the method exhibits highest sensitivity.[12,19] The key advantage of this method is the ability to derive absolute temperature, without requiring sensor calibration.[20] In general, in luminescence decay time thermometry, it is the decay time of the excited state that is used for temperature monitoring. Depopulation of the excited level can proceed *via*

[a]*Diamond Light Source, Harwell Campus, Didcot, OX11 0DE, UK. E-mail: vitaliy.mykhaylyk@diamond.ac.uk*
[b]*University of Oxford, Department of Physics, Denys Wilkinson Building, Keble Road, Oxford, OX1 3RH, UK*
[c]*Institute of Physics, Polish Academy of Sciences, Al. Lotnikow 32/46, Warsaw 02-668, Poland*
[d]*Lviv Polytechnic National University, 12 Bandera, Lviv 79013, Ukraine*

the radiative and the non-radiative path for which the rate can be a strong function of temperature. Thus, a value for temperature can be derived by measuring the rate of photons emitted *via* the radiative process. The thermal depopulation of the excited state through a non-radiative decay channel is the dominant process that determines the sensitivity of a probe over a broad temperature range.[14,21,22] Given that both techniques rely on a change in population of the excited state, they are complementary by nature and can be adopted within the same material. This idea gave rise to the concept of dual-mode sensing that is gaining in popularity.[23–28] Dual-mode sensing benefits from the possibility of cross-referencing sensor readings by using two methods, thereby improving reliability and accuracy of measurements. This concept received a fresh impetus recently when the feasibility of multimodal temperature sensing using three different techniques, *i.e.* intensity ratio, decay time and peak shift, was demonstrated in Cr-doped oxides.[29] Materials doped with transition metal ions are well suited for multimodal sensing owing to a noticeable shift of the luminescence peaks with temperature, caused by electron–phonon interaction of impurity ions with the host lattice.[30–32]

2. Concept of the multimodal dual-emitter sensor

A further performance enhancement of luminescence probes can be achieved by using a pair of emitters.[33] Combinations of different rare earth ions[34–37] as well as pairing rare-earth with transition metal ions[38–42] have been explored extensively and it has been shown that having two emitters in the same crystal enables a sensitivity enhancement and permits operation of the sensor over an extended temperature range. It is therefore important to assess this enhancement that a material with dual-emitters, multimodal sensor of temperature can bring, the topic of this feasibility study.

To employ all three schemes of temperature monitoring, including the shift of emission peaks as a function of temperature, hosts doped with two d^3-type transition metal ions are deemed to be most suitable because of the narrow band emission ($^2E \rightarrow {}^4A_2$) which depends on the strength of the crystal field. The application of single ions of Cr^{3+} or Mn^{4+} for triple temperature readout has been recently demonstrated.[29,32] Here we test the multimodal dual-emitter approach by co-doping Al_2O_3 with both these ions. Aluminium oxide is a stable material with simple structure and is comprehensively characterised as temperature sensor based on luminescence (see ref. 29 and reference herein). Moreover, Al_2O_3 is capable of accommodating transition metal ions in different valence states.[43–45] The sharp emission peaks of chromium and manganese ions observed at around 700 nm are strongly influenced by the crystal field environment and sensitive to variation of temperature. Thus, Al_2O_3 co-doped with Cr^{3+} and Mn^{4+} (Al_2O_3-Cr,Mn) represents an attractive material for these investigations. Here we will demonstrate how these two ions can be harnessed to enhance the performance of Al_2O_3 in temperature sensing applications.

It is pertinent to highlight that the dual-emitter approach in combination with the multimodal readout may offer an easy way of cross-referencing the selected temperature sensing method by a simple switch between the emission peaks of the activators. This offers an innovative solution to the cross-referencing and has as further advantage in-built redundancy of temperature sensing. The latter could provide a vital cross-check in critical applications due to being able to derive temperature from two emitters simultaneously without having to change the method of detection. Thus, this study is an important step towards the development of effective multifunctional thermometers with intrinsic redundancy of temperature sensing.

3. Experimental

3.1. Sample preparation

In this study we used powder samples of Al_2O_3 with nominal concentration of Mn = 0.02 at% and Cr = 0.005 at%, prepared *via* the sol–gel citrate route. These concentrations were selected based on our prior knowledge of the luminescence properties of the material, aiming to ensure that no energy transfer between the impurity ions occurs. As the ionic radius of Mn^{4+} (0.54 Å, CN = 6) is almost identical to that of Al^{3+} (0.53 Å, CN = 6) when doped into α-Al_2O_3 it can replace the Al^{3+} ions in the AlO_6 octahedra but requires charge compensation. This is achieved by the admixture of other ions in a 2+ valence state (typically Mg^{2+}).[46] Therefore Mg was added to the mixture in a concentration equal to that of Mn (0.02 at%). Water solutions of corresponding metal nitrates, taken in stoichiometric ratio according to nominal composition, were mixed together on a magnetic stirring device for 30 min. After that, the water solution of citric acid was added drop by drop to the reaction mixture, ensuring a molar ratio of metals to citric acid equal to 1 : 2. The solution prepared in this way was evaporated at a temperature of 80 °C and dried at 100 °C to form a polymer gel. The reaction occurs with intense release of NO_2 gas. The polymer gel was heat treated in several stages: at temperatures of 300 and 450 °C for 30 min to remove the organic component and at temperatures of 700, 800, 900 and 1000 °C with exposure at maximum temperature for 2 h. The final heat treatment of the product was performed at a temperature of 1200 °C for 4 h.

3.2. Luminescence characterisation

Photoluminescence characterization was performed using a Horiba/Jobin–Yvon Fluorolog-3 spectrofluorometer with a 450 W continuous spectrum xenon lamp for excitation. The emission was detected using a Hamamatsu R928P photomultiplier operating in photon counting mode. The luminescence decay kinetics were measured using the same Fluorolog-3 spectrofluorometer with the excitation light modulated by a mechanical modulator (chopper). The spectroscopic measurements in

the temperature range between 4.4 and 330 K were carried out in a Janis continuous-flow liquid-helium cryostat using a Lake Shore 331 temperature controller. The spectra presented here are corrected for the instrumental response of the detection system.

4. Results

4.1. X-ray diffraction and structure determination

Heat treatment of sol–gel derived precursors at 700 °C for 2 h leads to the formation of an X-ray amorphous product. Crystallization of the nanocrystalline γ-Al_2O_3 phase occurs after additional heating to 800 °C and this structure is preserved after further treatment at 900 °C. A well-crystallized α-Al_2O_3 corundum phase appears after further annealing of the material at 1000 °C for 2 h. Thus, the material heated to 1000 °C consists of two alumina polymorphs – nanocrystalline γ-Al_2O_3 and rhombohedral (sub)microcrystalline α-Al_2O_3 (Fig. 1). A practically pure corundum α-Al_2O_3 phase was obtained after additional heat treatment of the powder at 1200 °C for 4 h (see (Fig. 2)). Only few extra peaks with relative intensity less than 1% could be detected in the XRD pattern (*i.e.* at 27.6, 30.43, 31.88 and 44.65 deg. 2 theta), which, however, could not be identified among the phases containing Al–O–Mn–Mg.

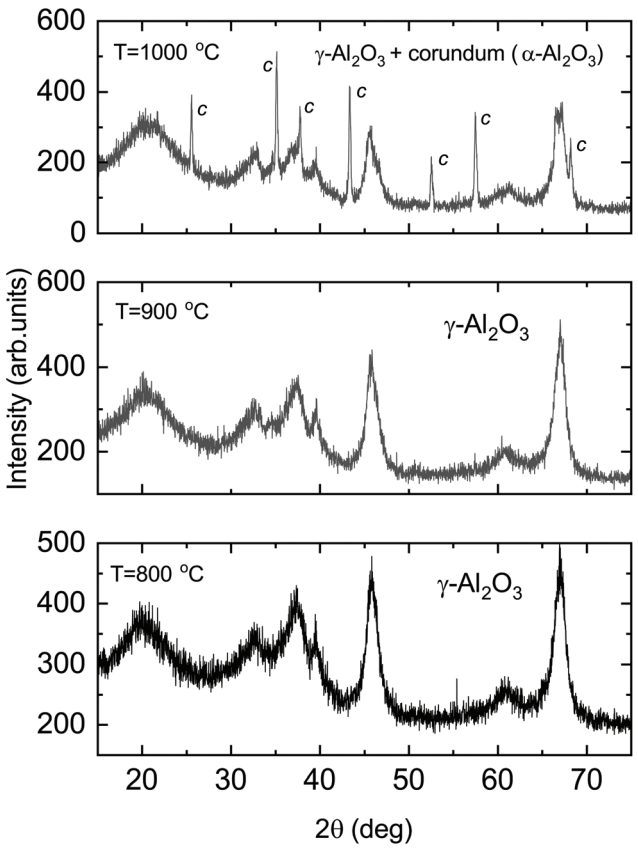

Fig. 1 X-ray diffraction patterns of sol–gel derived powders of Al_2O_3, subsequently heat treated in air at 800 °C, 900 °C and 1000 °C for 2 h.

The precise structural parameters of Al_2O_3 annealed at 1200 °C were derived by full profile Rietveld refinement from experimental XRD data collected over a wide 2Θ range, spanning 10 to 155° using an XPERT-PRO diffractometer. Unit cell dimensions, coordinates and isotropic displacement parameters of atoms in the rhombohedral Al_2O_3 structure were refined together with profile parameters, applying corrections for absorption and instrumental sample shift. As the final stage of the refinement procedure, anisotropic displacement parameters of Al and O species were refined. As a result, an excellent fit between calculated and experimental profiles was achieved (Fig. 2). Refined structural parameters of the final product and corresponding residuals are presented in Table 1.

4.2. Luminescence and crystal field analysis

Aluminium oxide doped with Cr^{3+} is an extensively studied material used as solid-state laser,[47] pressure sensor in diamond anvil cells[48] and sensor of temperature.[49,50] Therefore, the luminescence properties of this material and their temperature evolution are well documented (see *e.g.* ref. 29, 51, 52 and reference there). The studies of luminescence properties of Al_2O_3 doped with isoelectronic Mn^{4+} ions are, however, scarce. The low-temperature (T = 77 K) spectra due to $^2E \rightarrow {}^4A_2$ transitions in Al_2O_3-Mn^{4+} have been first reported by Geschwind *et al.*[44] and later the temperature changes of the luminescence were measured over the 2.5 to 295 K range.[53] It is worth commenting that the narrow band emission at 694 nm due to Cr^{3+} has been identified occasionally in samples of Mn^{4+}-doped Al_2O_3 [45,54] as such due to unintended contamination of the material.

The application of Al_2O_3-Cr,Mn as a dual-emitter probe for temperature sensing relies on a holistic understanding of processes governing the temperature changes of luminescence characteristics of the material. Therefore, we begin the study from measurements of the temperature-dependent spectroscopic characteristics. The luminescence excitation and emission spectra of Al_2O_3-Cr,Mn are shown in Fig. 3 while the positions of the main excitation bands and emission peaks of Cr^{3+} and Mn^{4+} are listed in Table 2.

The unfilled 3d states of Mn^{4+} and Cr^{3+} are strongly influenced by the immediate environment of the ions in the crystals. The crystal field causes a splitting of the electron states into several energy levels. The luminescence excitation bands due to $^4A_2 \rightarrow {}^4T_{2g}$, $^4T_{1g}$ transitions of Cr^{3+} are clearly identified at 557 and 405 nm. The luminescence excitation spectrum of Mn^{4+} consists of only two bands in the examined region. The band with a maximum at about 472 nm is related to the $^4A_2 \rightarrow {}^4T_{2g}$ transition and it is blue-shifted compared to the band associated with the same transitions for Cr^{3+} ions. The second band with a maximum at 390 nm is likely to be related to a mixture of $^4A_2 \rightarrow {}^4T_{1g}$ and charge-transfer transitions. We therefore assume that these two types of transitions spectrally overlap.

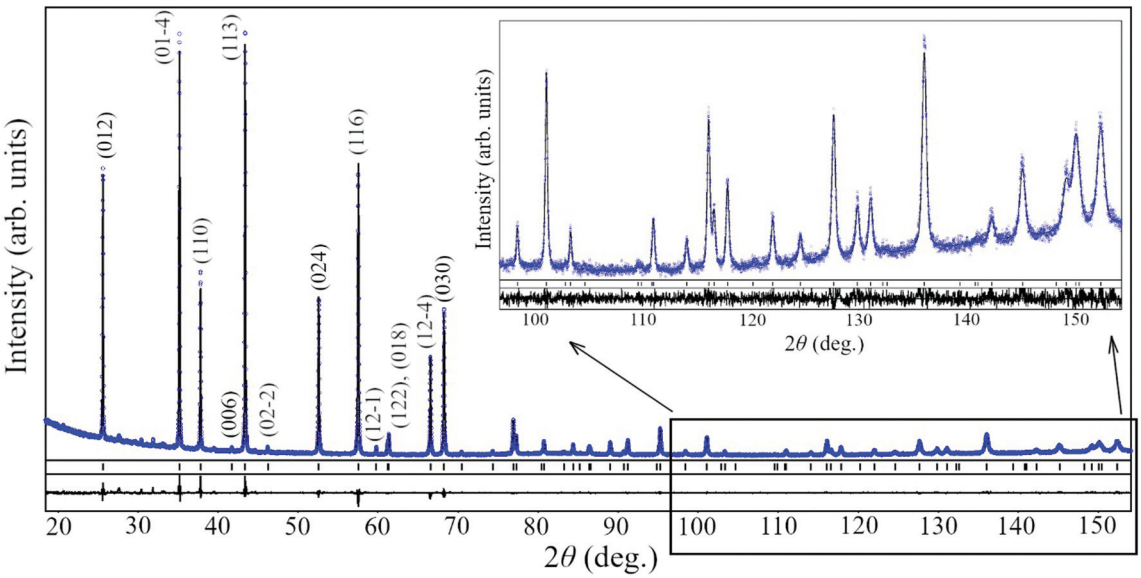

Fig. 2 Graphical results of Rietveld refinement of structure of Al_2O_3 annealed at 1200 °C in space group $R\bar{3}c$. Experimental and calculated XRD patterns (blue circles and black line, respectively) are shown together with corresponding Miller indices for Bragg maxima of the corundum structure. The inset shows the enlarged high-angle part of the pattern.

Table 1 Crystallographic data for Al_2O_3 annealed at 1200 °C: space group $R\bar{3}c$, a = 4.75931(6) Å, c = 12.9933(1) Å

Atoms, sites	x/a	y/b	z/c	$B_{iso/eq}$ [a], Å^2	B_{11}	B_{22}	B_{33}	B_{12}	B_{13}	B_{23}
Al, 12c	0	0	0.3524(1)	0.64(3)	0.61(3)	B_{11}	0.70(5)	$1/2B_{11}$	0	0
O, 18e	0.3080(4)	0	1/4	0.72(8)	0.70(8)	0.83(11)	0.66(10)	$1/2B_{22}$	−0.04(5)	$2B_{13}$

R_I = 0.028, R_P = 0.078

[a] $B_{iso/eq} = 1/3(B_{11}(a^*)^2a^2 + \ldots 2B_{23}b^*c^*bc\cos\alpha)$; $T = \exp(-1/4(B_{11}(a^*)^2h^2 + \ldots 2B_{23}b^*c^*kl))$.

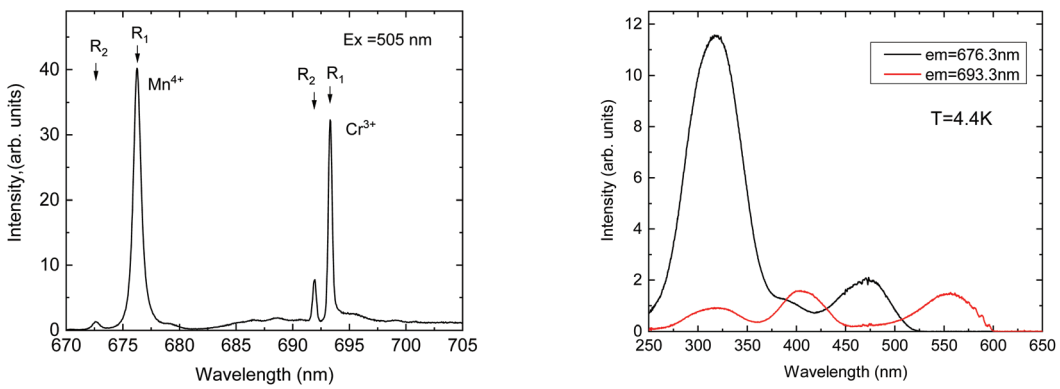

Fig. 3 Luminescence (left) and luminescence excitation spectra (right) of Al_2O_3-Cr,Mn measured at T = 40 K (emission) and 4.4 K (excitation).

Table 2 Position of Mn^{4+} and Cr^{3+} emission and excitation peaks in Al_2O_3 co-doped with Cr and Mn

Ion	$\bar{E} \rightarrow {}^4A_2$ (R_1-line), nm (cm^{-1})	$\overline{2A} \rightarrow {}^4A_2$ (R_2-line), nm (cm^{-1})	R_1–R_2 gap, meV (cm^{-1})	${}^4A_2 \rightarrow {}^4T_{1g}$ nm (cm^{-1})	${}^4A_2 \rightarrow {}^4T_{2g}$, nm ($cm^{-1}$)	Ref.
Mn^{4+}	676.3 (14 786)	672.6 (14 868)	10.1 (81.5)	390 (25 641)	472 (21 186)	This work
	676.3 (14 786)	672.7 (14 865)	10.2 (82.3)	320[a] (31 250)	470 (21 277)	44
Cr^{3+}	693.3 (14 424)	691.9 (14 453)	3.6 (29)	405 (24 691)	557 (17 953)	This work
	693.3 nm/(14 424)	691.9 (14 453)	3.6 (29)	411 (24 330)	568 (17 606)	29

[a] Tentative assignment due to overlap with the charge-transfer band.

Through knowing the positions of the bands it is possible to calculate the strength of the crystal field D_q and Racah parameters B and C, using the following formulas.[55]

$$E(^4T_{2g}) = 10D_q \quad (1)$$

$$\frac{B}{D_q} = \frac{\left(\frac{\Delta E}{D_q}\right)^2 - 10\left(\frac{\Delta E}{D_q}\right)}{15\left(\left(\frac{\Delta E}{D_q}\right) - 8\right)} \quad (2)$$

$$\frac{E(^2E_g)}{B} = \frac{3.05C}{B} + 7.9 - \frac{1.8B}{D_q} \quad (3)$$

$$\Delta E = E(^4T_{1g}) - E(^4T_{2g}) \quad (4)$$

For the calculations of crystal field parameters for Cr^{3+} we used band maxima positions. However, for Mn^{4+} reasonable values of crystal field and nephelauxetic parameter are obtained if, instead of band peaks, the expected positions of electronic levels (zero-phonon lines) are used. The overlap between the $^4A_2 \rightarrow {}^4T_{1g}$ and charge-transfer transitions for Mn^{4+} is responsible for difficulties in establishing the exact position of the $^4A_2 \rightarrow {}^4T_{1g}$ band. We assume that the positions of zero-phonon lines are located at the low-energy side of the appropriate bands. Parameters D_q, B, and C, calculated in this way, are listed in Table 3.

The results obtained also allow to calculate the nephelauxetic parameter β_1, defined in ref. 56 as:

$$\beta_1 = \sqrt{\left(\frac{B}{B_0}\right)^2 + \left(\frac{C}{C_0}\right)^2} \quad (5)$$

Having established the values of crystal field and Racah parameters, it is possible to construct Tanabe–Sugano diagrams for both ions. They are presented together in one figure (Fig. 4). The analysis of excitation spectra of Mn^{4+} and Cr^{3+} emission shows that the excitation bands of the two ions are well separated. No emission of Mn^{4+} is detected at the excitation in the range of the $^4A_2 \rightarrow {}^4T_{2g}$ band of Cr^{3+}, while the excitation spectrum of Cr^{3+} is similar to the one measured earlier in Al_2O_3-Cr[29] and exhibits no changes that could be attributed to the influence of other ions. This enables us to conclude that due to low concentration there is no energy transfer between dopant ions in the material under study that can markedly alter the luminescence characteristics.[41] Consequently, emission of Mn^{4+} and Cr^{3+} can be treated independently. This is an important condition that allows to analyse the changes of their luminescence characteristics with temperature within the framework of models developed for the emission of individual ions. The spectra also allowed to select a single wavelength for the excitation of both activators with the aim to achieve similar intensity of the R_1-lines.

The luminescence spectrum of Al_2O_3-Cr,Mn features two pairs of narrow peaks that correspond to the characteristic transitions of Mn^{4+} and Cr^{3+} (see (Fig. 3)). The peaks referred to as R_1 and R_2 lines are due to spin-forbidden transitions from the lowest excited ^2E level split into two levels ($\bar{E}$ and $\overline{2A}$) to the ground state $^4A_2$. The splitting is due to the lowering of the octahedral symmetry of the local crystal field surrounding the ions.[52] The magnitude of the splitting is proportional to the strength of the crystal field. The energy of the emission lines is further influenced by the nephelauxetic effect. The covalence increases with the charge of the ions,[56] resulting in an increase of the energy of the emitted photons. Consequently, the R-lines of Mn^{4+} are shifted to shorter wavelength with respect to the emission of Cr^{3+}. Notably, the correlation between the calculated nephelauxetic parameters β_1 and the position of the ^2E levels of the two ions fits the established trend.[56]

4.3. Temperature dependent luminescence characteristics

The high sensitivity of the outer 3d shells of Cr^{3+} and Mn^{4+} to changes of the crystal field environment and their coupling with lattice vibrations are the main factors that control the changes with temperature of the luminescence characteristics of ions in different hosts. Due to the very narrow emission peaks, a small change in the population of the emitting levels as wll as their energy is clearly visible in Fig. 5.

These changes are exploited by two methods of luminescence thermometry based on measurements of spectroscopic

Table 3 Crystal field and nephelauxetic β_1 parameters for Cr^{3+} and Mn^{4+} in Al_2O_3

	Value (cm^{-1})	
Parameter	Cr^{3+}	Mn^{4+}
D_q	1786	1905
B	714	762
C	3041	3038
β_1	1.0997	0.9573

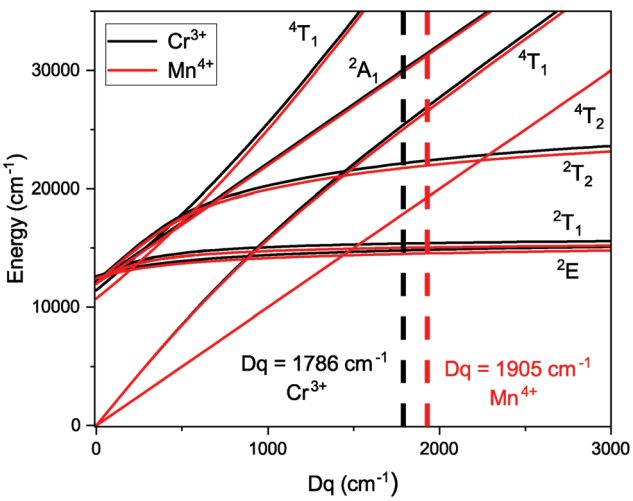

Fig. 4 Tanabe–Sugano diagrams for Cr^{3+} (black lines) and Mn^{4+} (red lines) in Al_2O_3. Positions of energy levels are slightly dependent on both B and C Racah parameters, therefore it is necessary to distinguish between Cr^{3+} and Mn^{4+}. The effect of the stronger crystal field for Mn^{4+} compared with that for Cr^{3+} is clearly visible on the graph.

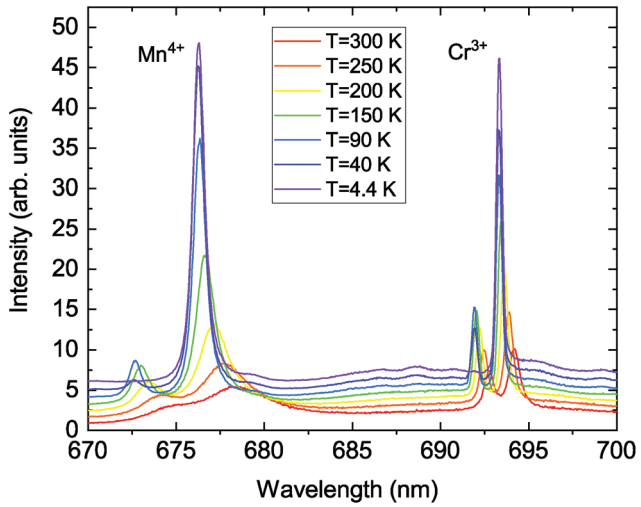

Fig. 5 Luminescence spectra of Al_2O_3 co-doped by Cr^{3+} and Mn^{4+} in the wavelength region of the R-lines, measured at 505 nm excitation and various temperatures. The spectra are shifted vertically for clarity.

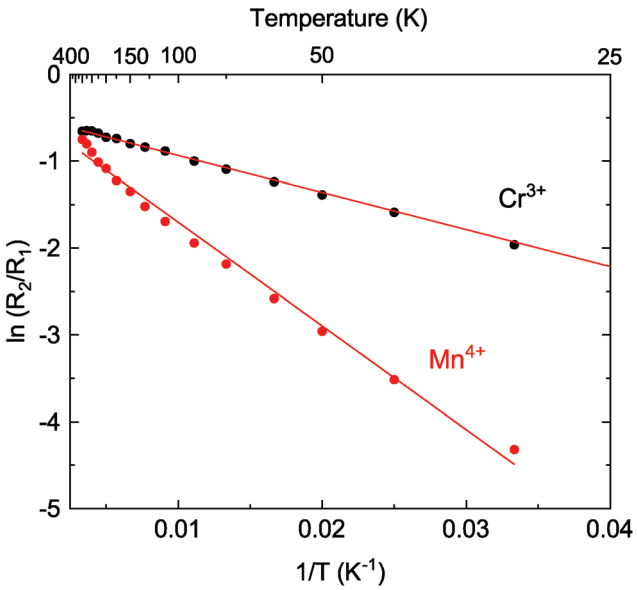

Fig. 6 Arrhenius plot for the intensity ratio of the R_2- and R_1-lines of Cr^{3+} and Mn^{4+} in Al_2O_3-Cr,Mn and linear fits of the dependences.

characteristics. Since the population of two emitting levels obeys Boltzmann statistics, the emission spectra exhibit a rapid decrease of the intensity of the R_2 lines with respect to R_1 at cooling due to an increase in the population of the lower exited state. In the framework of a statistical model, the ratio of intensities $F = I_{R_2}/I_{R_1}$ can be derived from the population of the levels in thermal equilibrium, resulting in the following expression:

$$F(T) = A \exp\left(-\frac{D}{kT}\right), \quad (6)$$

where A is a constant depending on the spontaneous emission rate, its frequency and degeneracy of the two levels,[20] D is the energy difference between the two emitting levels, k is the Boltzmann constant, and T is the absolute temperature. It should be noted that in some cases the background signal due to other emission processes can cause an offset, usually expressed through adding a constant to eqn (6).[19] The potential of a material as luminescence sensor of temperature can be assessed using the ratio of luminescence intensities of two lines. The Arrhenius plots displayed in Fig. 6 show good linearity above 30 K, evidencing thermal equilibrium between excited states in Mn^{4+} and Cr^{3+}. The deviation from linearity at high temperatures is due to thermalisation *via* phonon interaction not accounted for by the model. The values of energy gaps derived from a linear fit of the data are 3.67 ± 0.03 meV for Cr^{3+} and 10.2 ± 0.2 meV for Mn^{4+}. They correlate very well with the parameters obtained from spectroscopic measurements, confirming the validity of the underlying models. It is worthwhile noting that a factor of three difference in the energy gap is observed for the two ions, translating into different sensitivity of the intensity ratio to changes of temperature.

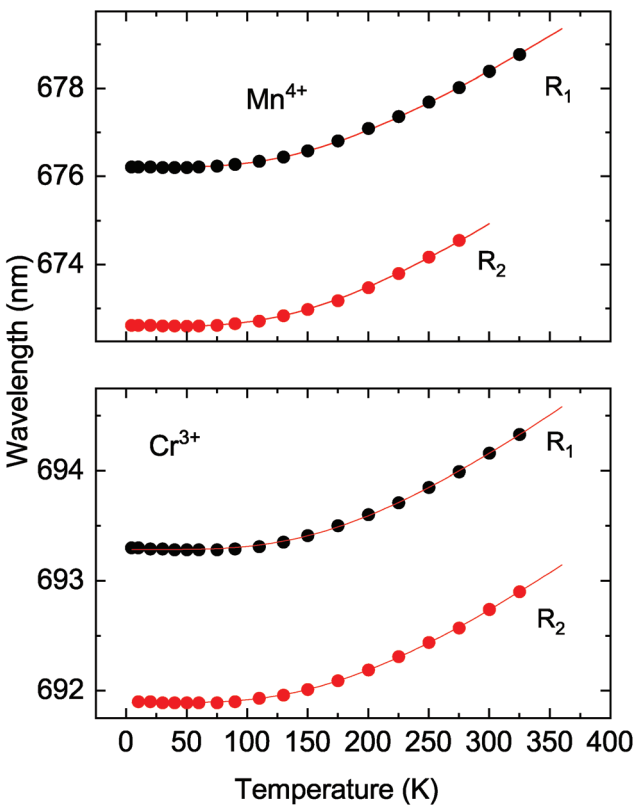

Fig. 7 Temperature shift of the R-lines of Mn^{4+} (top) and Cr^{3+} (bottom) in Al_2O_3-Cr,Mn measured at 505 nm excitation. The dots are the experimental data points and the solid lines show the best fit of experimental results to eqn (7), using parameters shown in Table 4.

The temperature dependence of the spectral position of the R_1 and R_2-lines are displayed in Fig. 7. The thermal shift of the lines, $\Delta\nu$, resulting from the interaction of electronic states of

impurity ions with acoustic phonons can be described by the Debye theory:[57]

$$\Delta\nu(T) = \alpha\left(\frac{T}{T_D}\right)^4 \int_0^{T_D/T} \frac{x^3}{\exp(x)-1}\,dx, \quad (7)$$

where α is the coupling coefficient for the electron–phonon interactions and T_D is the Debye temperature. We carried out a correlated fit of the R-line wave numbers for different temperatures to find the optimal values for the parameter α, individually for the two lines, and for the Debye temperature T_D, common to both datasets.

The applied fitting procedure resulted in very good fits throughout the entire measurement range. The fit parameters, summarised in Table 4, are in very good agreement with our recent results for Al_2O_3-Cr.[29] The value of the Debye temperature derived from the wavelength shift of Mn^{4+} is closer to earlier results for Al_2O_3-Cr, T_D = 750 K.[57] It should be noted that the R-lines of both ions exhibit a very similar pattern regarding the spectral shift with temperature. The shift is negligible below 100 K while it can be detected at temperature above that, thus confining this temperature monitoring method to temperatures above 100 K.

Table 4 Parameters of fits obtained from the temperature dependence of the luminescence wavelength shift eqn (3) for Cr^{3+} and Mn^{4+} emission in Al_2O_3-Cr,Mn

Parameter	Cr^{3+} in Al_2O_3-Cr	Cr^{3+} in Al_2O_3-Cr,Mn	Mn^{4+} in Al_2O_3-Cr,Mn
α_{R_1}, cm^{-1}	−518.0	−515.2	−1048.5
α_{R_2}, cm^{-1}	−507.5	−500.0	−972.0
T_D, K	867	856	736
Ref.	29	This work	This work

One more method of temperature monitoring that can be implemented with materials doped with transition metal ions uses the luminescence decay time of the R-lines. To evaluate the merit of the dual-emitter concept of temperature sensing further we investigated the changes of the luminescence decay time with temperature of Cr^{3+} and Mn^{4+} in Al_2O_3. Fig. 8 shows the decay curves recorded at 694 and 676 nm peaks and temperature dependence of respective decay time constants.

Qualitatively the measured dependences are very similar for both ions. The initial increase of the decay time constant with cooling can be readily explained by the decrease of the probability for non-radiative de-excitation of the emitting level. This is a typical behaviour observed in luminescence materials.[58,59] The decay time constant reaches a maximum value at *ca.* 100 K but below this temperature it decreases with further cooling. Such drop of $\tau = f(T)$ at very low temperatures is not very common. It has been discussed so far in few materials doped with Cr^{3+} (ref. 29, 60 and 61) while it is the

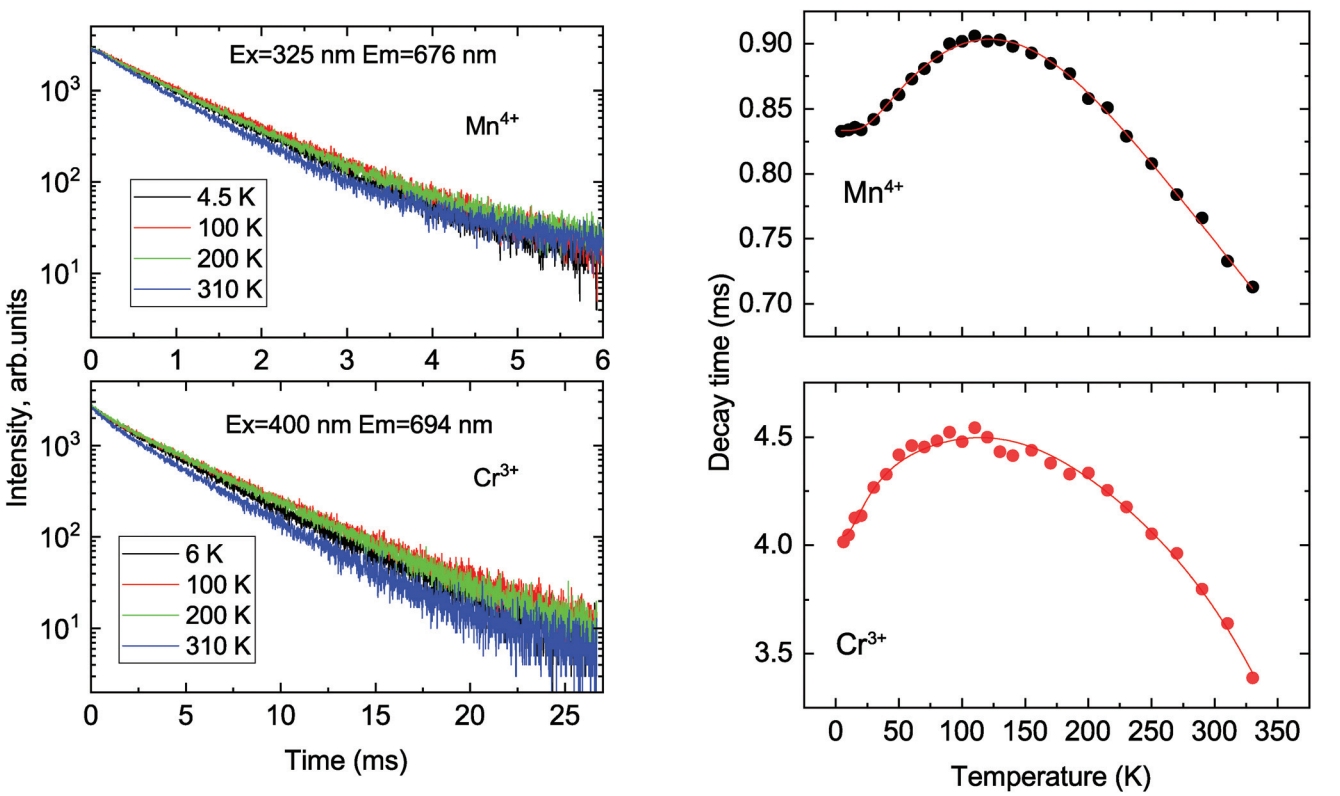

Fig. 8 Left – Decay curves measured at the peak of Mn^{4+} and Cr^{4+} emission at different temperatures. Right – Temperature dependence of the luminescence decay time constant of Mn^{4+} (top) and Cr^{3+} emission (bottom) in Al_2O_3-Cr,Mn. The solid lines show the best fit of eqn (8) to the experimental results (dots) using the parameters summarised in Table 5.

first time that the effect is explicitly observed for Mn^{4+} emission. This behaviour is explained assuming different radiative transition probability from the $\bar{E}$ and $\overline{2A}$ levels, constituting the emitting ^2E state. The probability of radiative decay from the upper level $(\overline{2A})$ is lower in comparison with that for $\bar{E}$, leading to an increase of the measured radiative decay time constant of the R-line emission. However, a decrease of temperature leads to depopulation of the upper level, thereby reducing its contribution to the emission process in favour of transitions from the low-lying level $\bar{E}$ with a higher radiative decay rate. This is then manifested as decrease of the measured decay time constant of the R-lines with further cooling.

The observed behaviour of the decay time constant for the Cr^{3+} and Mn^{4+} emissions in Al_2O_3 over the examined temperature range reflects the dynamic of temperature changes in the population of the excited states and probabilities of transitions between them. Recently we demonstrated that this convoluted phenomenon can be comprehensively described by taking into account the main processes affecting the population and radiative rates of the ^2E state, *i.e.* thermalisation, phonon-assisted interaction with lattice vibrations and thermally induced depopulation.[29] Under the assumption of thermal equilibrium between the states $\bar{E}$, $\overline{2A}$ and $^4T_2$ involved in the transitions and considering interactions with lattice vibrations we obtained the following expression for $\tau(T)$:

$$\tau(T) = \frac{1 + \exp\left(-\frac{D}{kT}\right) + 6\exp\left(-\frac{\Delta E}{kT}\right)}{\frac{1}{\tau_1}\coth\left(\frac{E_p}{2kT}\right) + \frac{1}{\tau_2}\coth\left(\frac{E_p}{2kT}\right)\exp\left(-\frac{D}{2kT}\right) + \frac{6}{\tau_3}\exp\left(-\frac{\Delta E}{kT}\right)}. \quad (8)$$

Here $1/\tau_i$ (i = 1, 2 and 3) are the radiative decay rates of the $\bar{E}$, $\overline{2A}$, and $^4T_2$ levels respectively. ΔE is the energy difference between the ^2E and $^4T_2$ levels, E_p stands for "effective energy" of the phonons responsible for the exchange with the sidebands while other notations are explained above. This equation explicitly describes the thermalisation process occurring between the $\bar{E}$ and $\overline{2A}$ levels, phonon-assisted relaxation and depopulation of the levels due to thermally induced $^2E \rightarrow {}^4T_2$ transitions.

As shown in Fig. 8 the measured temperature dependences of the decay time constants of Cr^{3+} and Mn^{4+} perfectly fit the equation confirming agreement of experimental results with theory over the entire temperature range. The parameters of the fit for Cr^{3+} summarised in Table 5 show good agreement with the results published earlier while the effective energy of phonons, E_p, is comparable with the mean value of the phonon energy of Al_2O_3.[62]

It should be noted that from the standpoint of temperature monitoring the observed change in the slope of the $\tau = f(T)$ curve is worse in comparison with temperature dependences of other luminescence characteristics that exhibit a monotonous trend. This change is caused by a lower sensitivity of the method around the peak of the curve. The consequences and implication of this feature for the dual-emitter sensing will be discussed in the next section.

Table 5 Fit parameters obtained from the temperature dependence of the luminescence decay time constant eqn (5) for Cr^{3+} and Mn^{4+} emission in Al_2O_3-Cr,Mn

Parameter	Cr^{3+} in Al_2O_3-Cr	Cr^{3+} in Al_2O_3-Cr,Mn	Mn^{4+} in Al_2O_3-Cr,Mn
τ_1, ms	3.98 ± 0.01	4.04 ± 0.01	0.83 ± 0.01
τ_2, ms	4.46 ± 0.01	5.43 ± 0.02	1.16 ± 0.01
E_p, meV	60.9 ± 0.4	61.2 ± 0.1	55.7 ± 0.1
D^a, meV	3.6	3.6	10.2
τ_3, μs	33 ± 25	86 ± 41	139 ± 94
ΔE, meV	237 ± 23	281 ± 15	213 ± 25
Ref.	29	This work	This work

[a] The value of D is fixed to be equal to the energy splitting of the ^2E level.

4.4. Thermometric performance

To estimate the merit of a dual-emitter Al_2O_3-Cr,Mn probe in different modes of temperature sensing we adopted as metrics the temperature uncertainty δT. This parameter calculated by converting the uncertainty of the parameter that is measured, δQ, by dividing it by the responsivity of the sensor, $|dQ/dT|$.[18,63,64]

$$\delta T = \delta Q\left|\frac{dQ}{dT}\right|^{-1}. \quad (9)$$

This approach allows a direct comparison of the different temperature measurement methods.[29]

The absolute sensitivity can be readily calculated from the measured temperature dependence of the parameter of interest. The uncertainty of the measurements of decay time and intensity ratio over the examined temperature range were estimated to be 0.5% and 2% respectively. The absolute error in determining the wavelength shift is taken as a constant value of 0.02 nm. These data were used to calculate the uncertainty of temperature measurements $\delta T = f(T)$ for different modes of sensing (see Fig. 9).

Analysis of the plots allows to assess the potential of the multimodal dual-emitter concept as non-contact luminescence sensor of temperature. The plot clearly demonstrates the significant difference in the achievable resolution depending on the measurement technique, luminescence ion and temperature range of operation. The lowest temperature uncertainty (±0.1 K at 10 K) can be reached by using the intensity ratio of R-lines of Cr^{3+} while for Mn^{4+} emission this value is three times higher. The sensitivity of the method is proportional to the energy gap between the R-levels involved in the transitions[19,20] translating to better temperature resolution achievable with Cr^{3+} ions in comparison with Mn^{4+}. However, a smaller gap also implies a narrow temperature range for a ratiometric sensor.[20] This shortcoming of the intensity ratio method using Cr^{3+} emission is clearly visible in Fig. 9. The measurement uncertainty increases very rapidly; it is more than ±1 K above 50 K. In this regard the intensity ratio of the R-lines of Mn^{4+} is superior in comparison with other tech-

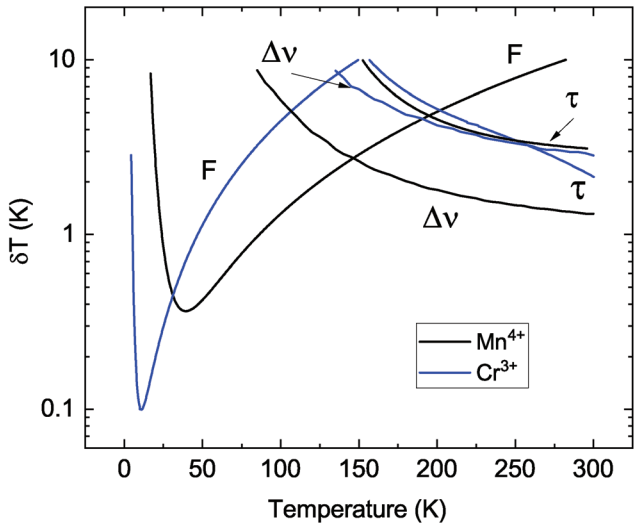

Fig. 9 The temperature resolution of Al_2O_3-Cr,Mn in different modes of temperature sensing: F – luminescence intensity ratio, $\Delta\nu$ – spectral shift and τ – decay time constant.

niques as such, permitting to achieve lowest uncertainty of temperature measurements over the 40–145 K range.

Inspecting Fig. 9 shows that the temperature monitoring techniques based on intensity ratio and wavelength shift of the Mn^{4+} emission exhibit the same uncertainty of ±2.8 K at about T = 145 K. This defines a cross-over point between the two methods. It is worthwhile noting that for Cr^{3+} emission the measurement uncertainty at the cross-over point (T = 135 K) is larger by a factor three. At higher temperatures (145–300 K) the best temperature resolution can be achieved by monitoring the wavelength shift of the R-lines of the Mn^{4+} luminescence. This gives more accurate readings in comparison with the shift of Cr^{3+} lines and methods based on the changes of decay time constants of Cr^{3+} or Mn^{4+} emission. The R-lines of Mn^{4+} exhibit a larger shift with temperature in comparison to Cr^{3+} lines (see also Fig. 5), translating into better accuracy. It is also evident that the temperature resolution of decay time thermometry in this case is inferior when compared with spectroscopic methods of temperature monitoring. Finally, it should be noted that temperature resolution obtained for Al_2O_3 co-doped with Cr^{3+} and Mn^{4+} is very compatible with the typical values reported for other oxides doped with transition metal ions (see Table 6).

Table 6 Thermometric resolution of Cr^{3+} and Mn^{4+} doped oxides

Material	Method	Temperature, K	Temperature resolution, K	Ref.
α-Al_2O_3-Cr	Intensity ratio	30	0.45	63
α-Ga_2O_3-Cr	Intensity ratio	300	0.25	65
β-Ga_2O_3-Cr	Intensity ratio	300	0.42	65
β-Ga_2O_3-Cr	Line shift	300	2	29
β-Ga_2O_3-Cr	Decay time	165	0.3	29
$YAlO_3$-Cr	Intensity ratio	20	0.2	29
$Bi_2Al_4O_9$-Cr	Intensity ratio	300	0.23	66
Mg_2SiO_4-Cr	Line shift	310	7.9	32
Mg_2SiO_4-Cr	Decay time	310	0.2	32
Li_2TiO_3-Mn	Decay time	332	0.032	67
Zn_2GeO_4-Mn	Decay time	360	0.64	26
$MgTiO_3$-Mn	Intensity ratio	93	0.42	24
$MgTiO_3$-Mn	Decay time	278	0.025	24

5. Conclusion

The concept of multimodal dual-emitter luminescence sensors of temperature was put to the test using Al_2O_3 co-doped with transition metal ions of Cr^{3+} and Mn^{4+}. To assess the feasibility of non-contact temperature measurements through monitoring the intensity ratio, wavelength shift, and decay time constant of R-lines emitted by both ions, we examined the evolution of the luminescence spectra and decay time constant of Al_2O_3-Cr,Mn over the 4–350 K temperature range. Detailed analysis of spectroscopic results allowed to determine the energy level diagram and establish that the crystal field acting upon each ion governs the luminescence properties of the material. The investigations were conducted by comparing experiments with relevant theoretical models. It is shown that the models provide adequate interpretation of the emission processes, evidenced by the high quality of fits obtained for the measured temperature dependences of the luminescence intensity ratio, wavelength shift and decay time constant for both emitting ions.

The thermometric performance of Al_2O_3-Cr,Mn was assessed by analysing the temperature resolution achievable by different methods. The comparison shows that in this material the resolution obtained through measuring the luminescence decay time constant is not adequate for monitoring temperature over 4–300 K range. In contrast, the intensity ratio method is superior at very low temperature as it allows to attain a temperature uncertainty as low as ±0.1 K at 10 K by monitoring Cr^{3+} emission. As temperature increases, measurements of the intensity ratio of the R-lines of Mn^{4+} is preferable as such, giving better accuracy in comparison with that of Cr^{3+} emission. Though the accuracy of the method gradually decreases it remains the most accurate up to the cross-over point at 145 K when the measurement uncertainty reaches ±2.8 K. Above this point monitoring the wavelength shift of Mn^{4+} lines allows the temperature to be determined with better uncertainty.

The significance of these findings is two-fold. First, they demonstrated the viability of the dual-emitter multimodal concept for non-contact luminescence measurements of temperature. The luminescence characteristics of transition metal ions co-doped in Al_2O_3 exhibit measurable changes with temperature, laying the foundation for future designs of novel materials and read-out configurations with improved accuracy and reliability. Second, the results of this study highlighted the advantage of Mn^{4+} emission in aluminium oxide for thermometric application. It is very competitive in comparison with Cr-doped Al_2O_3 and consequently this material holds a

considerable promise for the technology of non-contact sensing.

Conflicts of interest

There are no conflicts to declare.

Acknowledgements

The work was partially supported by the Polish National Science Centre (project no. 2018/31/B/ST8/00774) and by the National Research Foundation of Ukraine (grant no. 2020.02/0373).

Notes and references

1 S. W. Allison and G. T. Gillies, Remote thermometry with thermographic phosphors: Instrumentation and applications, *Rev. Sci. Instrum.*, 1997, **68**, 2615–2650.
2 N. Fuhrmann, T. Kissel, A. Dreizler and J. Brubach, Gd3Ga5O12:Cr-a phosphor for two-dimensional thermometry in internal combustion engines, *Meas. Sci. Technol.*, 2011, **22**, 045301.
3 V. B. Mykhaylyk, H. Kraus and A. Wagner, Non-Contact Luminescence Lifetime Microthermometry using Scintillation Sensors, *Acta Phys. Pol., A*, 2018, **133**, 1108–1111.
4 A. H. Khalid, K. Kontis and H. Z. Behtash, Phosphor thermometry in gas turbines: consideration factors, *Proc. Inst. Mech. Eng., Part G*, 2010, **224**, 745–755.
5 T. Hartman, R. G. Geitenbeek, C. S. Wondergem, W. van der Stam and B. M. Weckhuysen, Operando Nanoscale Sensors in Catalysis: All Eyes on Catalyst Particles, *ACS Nano*, 2020, **14**, 3725–3735.
6 A. J. Warren, D. Axford and R. L. Owen, Direct measurement of X-ray-induced heating of microcrystals, *J. Synchrotron Radiat.*, 2019, **26**, 991–997.
7 X. J. Zhu, W. Feng, J. Chang, Y. W. Tan, J. C. Li, M. Chen, Y. Sun and F. Y. Li, Temperature-feedback upconversion nanocomposite for accurate photothermal therapy at facile temperature, *Nat. Commun.*, 2016, **7**, 10437.
8 K. Okabe, N. Inada, C. Gota, Y. Harada, T. Funatsu and S. Uchiyama, Intracellular temperature mapping with a fluorescent polymeric thermometer and fluorescence lifetime imaging microscopy, *Nat. Commun.*, 2012, **3**, 705.
9 T. Hayashi, N. Fukuda, S. Uchiyama and N. Inada, A Cell-Permeable Fluorescent Polymeric Thermometer for Intracellular Temperature Mapping in Mammalian Cell Lines, *PLoS One*, 2015, **10**, e0117677.
10 C. D. S. Brites, P. P. Lima, N. J. O. Silva, A. Millan, V. S. Amaral, F. Palacio and L. D. Carlos, Thermometry at the nanoscale, *Nanoscale*, 2012, **4**, 4799–4829.
11 T. T. Bai and N. Gu, Micro/Nanoscale Thermometry for Cellular Thermal Sensing, *Small*, 2016, **12**, 4590–4610.
12 X. D. Wang, O. S. Wolfbeis and R. J. Meier, Luminescent probes and sensors for temperature, *Chem. Soc. Rev.*, 2013, **42**, 7834–7869.
13 B. del Rosal, E. Ximendes, U. Rocha and D. Jaque, In Vivo Luminescence Nanothermometry: from Materials to Applications, *Adv. Opt. Mater.*, 2017, **5**, 1600508.
14 M. D. Dramicanin, Trends in luminescence thermometry, *J. Appl. Phys.*, 2020, **128**, 040902.
15 J. J. Zhou, B. del Rosal, D. Jaque, S. Uchiyama and D. Y. Jin, Advances and challenges for fluorescence nanothermometry, *Nat. Methods*, 2020, **17**, 967–980.
16 J. D. A. Bednarkiewicz, K. Trejgis, D. Jaque, E. Ximendes and L. Marciniak, Luminescence based temperature bioimaging: Status, challenges, and perspectives, *Appl. Phys. Rev.*, 2021, **8**, 011317.
17 J. W. Kenney and J. J. Lee, Photoluminescent Metal Complexes and Materials as Temperature Sensors-An Introductory Review, *Chemosensors*, 2021, **9**, 109.
18 C. D. S. Brites, S. Balabhadra and L. D. Carlos, Lanthanide-Based Thermometers: At the Cutting-Edge of Luminescence Thermometry, *Adv. Opt. Mater.*, 2019, **7**, 1801239.
19 S. A. Wade, S. F. Collins and G. W. Baxter, Fluorescence intensity ratio technique for optical fiber point temperature sensing, *J. Appl. Phys.*, 2003, **94**, 4743–4756.
20 M. Suta and A. Meijerink, A Theoretical Framework for Ratiometric Single Ion Luminescent Thermometers-Thermodynamic and Kinetic Guidelines for Optimized Performance, *Adv. Theory Simul.*, 2020, **3**, 2000176.
21 M. D. Chambers and D. R. Clarke, Doped Oxides for High-Temperature Luminescence and Lifetime Thermometry, *Annu. Rev. Mater. Res.*, 2009, **39**, 325–359.
22 S. Yakunin, B. M. Benin, Y. Shynkarenko, O. Nazarenko, M. I. Bodnarchuk, D. N. Dirin, C. Hofer, S. Cattaneo and M. V. Kovalenko, High-resolution remote thermometry and thermography using luminescent low-dimensional tin-halide perovskites, *Nat. Mater.*, 2019, **18**, 846–852.
23 J. S. Zhong, D. Q. Chen, Y. Z. Peng, Y. D. Lu, X. Chen, X. Y. Li and Z. G. Ji, A review on nanostructured glass ceramics for promising application in optical thermometry, *J. Alloys Compd.*, 2018, **763**, 34–48.
24 E. Glais, V. Dordevic, J. Papan, B. Viana and M. D. Dramicanin, MgTiO3:Mn4+ a multi-reading temperature nanoprobe, *RSC Adv.*, 2018, **8**, 18341–18346.
25 S. Gharouel, L. Labrador-Paez, P. Haro-Gonzalez, K. Horchani-Naifer and M. Ferid, Fluorescence intensity ratio and lifetime thermometry of praseodymium phosphates for temperature sensing, *J. Lumin.*, 2018, **201**, 372–383.
26 F. F. Chi, B. Jiang, Z. M. Zhao, Y. H. Chen, X. T. Wei, C. K. Duan, M. Yin and W. Xu, Multimodal temperature sensing using Zn2GeO4:Mn2+ phosphor as highly sensitive luminescent thermometer, *Sens. Actuators, B*, 2019, **296**, 126640.
27 L. Marciniak, K. Elzbieciak-Piecka, K. Kniec and A. Bednarkiewicz, Assessing thermometric performance of

Sr2CeO4 and Sr2CeO4:Ln(3+) (Ln(3+) = Sm3+, Ho3+, Nd3+, Yb3+) nanocrystals in spectral and temporal domain, *Chem. Eng. J.*, 2020, **388**, 124347.

28 M. Sojka, C. D. S. Brites, L. D. Carlos and E. Zych, Exploiting bandgap engineering to finely control dual-mode Lu-2(Ge,Si)O-5:Pr(3+)luminescence thermometers, *J. Mater. Chem. C*, 2020, **8**, 10086–10097.

29 V. Mykhaylyk, H. Kraus, Y. Zhydachevskyy, V. Tsiumra, A. Luchechko, A. Wagner and A. Suchocki, Multimodal Non-Contact Luminescence Thermometry with Cr-Doped Oxides, *Sensors*, 2020, **20**, 5259.

30 D. Pugh-Thomas, B. M. Walsh and M. C. Gupta, Spectroscopy of BeAl2O4:Cr3+ with application to high-temperature sensing, *Appl. Opt.*, 2010, **49**, 2891–2897.

31 S. Adachi, Review-Mn4+-Activated Red and Deep Red-Emitting Phosphors, *ECS J. Solid State Sci. Technol.*, 2019, **9**, 016001.

32 Z. Risti, V. Dordevic, M. Medic, S. Kuzman, M. Sekulic, Z. Antic and M. D. Dramicanin, Triple-temperature readout in luminescence thermometry with Cr3+-doped Mg2SiO4 operating from cryogenic to physiologically relevant temperatures, *Meas. Sci. Technol.*, 2021, **32**, 054004.

33 J. McLaurin, L. R. Bradshaw and D. R. Gamelin, Dual-Emitting Nanoscale Temperature Sensors, *Chem. Mater.*, 2013, **25**, 1285–1292.

34 M. K. Mahata, T. Koppe, K. Kumar, H. Hofsass and U. Vetter, Demonstration of Temperature Dependent Energy Migration in Dual-Mode YVO4: Ho3+/Yb3+ Nanocrystals for Low Temperature Thermometry, *Sci. Rep.*, 2016, **6**, 36342.

35 Y. Xu, Z. Sun, Y. L. Wei, M. C. Jia, B. F. Hou, X. Li, F. Lin, M. X. Zhang, H. Y. Wang and Z. L. Fu, Optical properties of the CaEuAl(3)O(7)phosphor with dual-activator Eu2+/Eu (3+)for multifunctional applications, *J. Am. Ceram. Soc.*, 2020, **103**, 5721–5730.

36 H. L. Song, C. Wang, Q. Han, X. Y. Tang, W. C. Yan, Y. F. Chen, J. F. Jiang and T. G. Liu, Highly sensitive Tm3+/Yb3+ codoped SrWO4 for optical thermometry, *Sens. Actuators, A*, 2018, **271**, 278–282.

37 Z. H. Fang, L. Zhao, Q. H. Yang, Z. Yang, Y. Y. Cai, D. C. Zhou, X. Yu, J. B. Qiu and X. H. Xu, Optical thermometry properties of silicate glass ceramics with dual-phase for spatial isolation of Er3+ and Cr3+, *J. Lumin.*, 2020, **219**, 116861.

38 D. Q. Chen, S. Liu, Y. Zhou, Z. G. Wan, P. Huang and Z. G. Ji, Dual-activator luminescence of RE/TM:Y3Al5O12 (RE = Eu-3+,Eu- Tb3+, Dy3+; TM = Mn4+, Cr3+) phosphors for self-referencing optical thermometry, *J. Mater. Chem. C*, 2016, **4**, 9044–9051.

39 Y. B. Chen, J. He, X. G. Zhang, M. C. Rong, Z. G. Xia, J. Wang and Z. Q. Liu, Dual-Mode Optical Thermometry Design in Lu3Al5O12:Ce3+/Mn4+ Phosphor, *Inorg. Chem.*, 2020, **59**, 1383–1392.

40 C. Y. Xie, L. Zhao, B. Jiang, J. S. Mao, Y. Lin, P. Wang, X. T. Wei, M. Yin and Y. H. Chen, Dual-activator luminescence of LuAG:Mn4+/Tb3+ phosphor for optical thermometry, *J. Am. Ceram. Soc.*, 2019, **102**, 7500–7508.

41 W. Piotrowski, K. Kniec and L. Marciniak, Enhancement of the Ln3+ ratiometric nanothermometers by sensitization with transition metal ions, *J. Alloys Compd.*, 2021, **870**, 159386.

42 K. Elzbieciak-Piecka, M. Suta and L. Marciniak, Structurally induced tuning of the relative sensitivity of LaScO3:Cr3+ luminescent thermometers by co-doping lanthanide ions, *Chem. Eng. J.*, 2021, **421**, 129757.

43 W. H. Fonger and C. W. Struck, Temperature dependences of Cr+ 3 radiative and nonradiative transitions in ruby and emerald, *Phys. Rev. B: Solid State*, 1975, **11**, 3251–3260.

44 S. Geschwind, P. Kisliuk, M. P. Klein, J. Remeika and D. L. Wood, Sharp-Line Fluorescence, Electron Paramagnetic Resonance, and Thermoluminescence of Mn 4+ in α-Al2O3, *Phys. Rev.*, 1962, **126**, 1684–1686.

45 C. Tian, H. Lin, D. W. Zhang, P. P. Zhang, R. J. Hong, Z. X. Han, X. L. Qian and J. Zou, Mn-4(+) activated Al2O3 red-emitting ceramic phosphor with excellent thermal conductivity, *Opt. Express*, 2019, **27**, 32666–32678.

46 M. G. Brik, Y. X. Pan and G. K. Liu, Spectroscopic and crystal field analysis of absorption and photoluminescence properties of red phosphor CaAl12O19:Mn4+ modified by MgO, *J. Alloys Compd.*, 2011, **509**, 1452–1456.

47 B. Denker and E. Shklovsky, *Handbook of Solid-State Lasers: Materials, Systems and Applications*, Woodhead Publishing, Cambridge, 2013.

48 F. Datchi, A. Dewaele, P. Loubeyre, R. Letoullec, Y. Le Godec and B. Canny, Optical pressure sensors for high-pressure-high-temperature studies in a diamond anvil cell, *High Pressure Res.*, 2007, **27**, 447–463.

49 F. Anghel, C. Iliescu, K. T. V. Grattan, A. W. Palmer and Z. Y. Zhang, Fluorescent-Based Lifetime Measurement Thermometer for Use at Subroom Temperatures (200–300 K), *Rev. Sci. Instrum.*, 1995, **66**, 2611–2614.

50 K. T. V. Grattan, Z. Y. Zhang, T. Sun, Y. H. Shen, L. M. Tong and Z. C. Ding, Sapphire-ruby single-crystal fibre for application in high temperature optical fibre thermometers: studies at temperatures up to 1500 degrees C, *Meas. Sci. Technol.*, 2001, **12**, 981–986.

51 D. D. Ragan, R. Gustavsen and D. Schiferl, Calibration of the Ruby R(1) and R(2) Fluorescence Shifts as a Function of Temperature from 0 to 600-K, *J. Appl. Phys.*, 1992, **72**, 5539–5544.

52 R. C. Powell, *Physics of Solid-State Laser Materials*, Springer-Verlag, New York, 1998.

53 H. Riesen, T. Monks-Corrigan and N. B. Manson, Temperature dependence of the R-1 linewidth in Al2O3: Mn4+: A spectral hole-burning and FLN study, *Chem. Phys. Lett.*, 2011, **515**, 241–244.

54 I. V. Gasenkova, N. I. Mukhurov, S. P. Zhvavyi, E. E. Kolesnik and A. P. Stupak, Photoluminescent properties of nanoporous anodic alumina doped with manganese ions, *J. Lumin.*, 2017, **185**, 298–305.

55 B. Henderson and G. F. Imbush, *Optical Spectroscopy of Inorganic Solids*, Oxford University Press, Oxford, 1989.

56 M. G. Brik, S. J. Camardello, A. M. Srivastava, N. M. Avram and A. Suchocki, Spin-Forbidden Transitions in the Spectra

of Transition Metal Ions and Nephelauxetic Effect, *ECS J. Solid State Sci. Technol.*, 2016, **5**, R3067–R3077.

57 D. E. McCumber and M. D. Sturge, Linewidth and Temperature Shift of the R Lines in Ruby, *J. Appl. Phys.*, 1963, **34**, 1682–1684.

58 G. Blasse and B. C. Grambaier, *Luminescence Materials*, Springer-Verlag Berlin, Heidelberg, 1994.

59 N. Ahmed, H. Kraus, H. J. Kim, V. Mokina, V. Tsiumra, A. Wagner, Y. Zhydachevskyy and V. B. Mykhaylyk, Characterisation of tungstate and molybdate crystals ABO4 (A=Ca, Sr, Zn, Cd; B=W, Mo) for luminescence lifetime cryothermometry, *Materialia*, 2018, **4**, 287–296.

60 D. F. Nelson and M. D. Sturge, Relation between Absorption and Emission in the Region of the R- Lines of Ruby, *Phys. Rev.*, 1965, **137**, A1117–A1130.

61 Z. Y. Zhang, K. T. V. Grattan and A. W. Palmer, Temperature Dependences of Fluorescence Lifetimes in Cr-3+-Doped Insulating Crystals, *Phys. Rev. B: Condens. Matter Mater. Phys.*, 1993, **48**, 7772–7778.

62 Z. Lodziana and K. Parlinski, Dynamical stability of the alpha and theta phases of alumina, *Phys. Rev. B: Condens. Matter Mater. Phys.*, 2003, **67**, 174106.

63 M. Back, J. Ueda, M. G. Brik and S. Tanabe, Pushing the Limit of Boltzmann Distribution in Cr3+-Doped CaHfO3 for Cryogenic Thermometry, *ACS Appl. Mater. Interfaces*, 2020, **12**, 38325–38332.

64 V. B. Mykhaylyk, H. Kraus, L. Bobb, R. Gamernyk and K. Koronski, Megahertz non-contact luminescence decay time cryothermometry by means of ultrafast PbI2 scintillator, *Sci. Rep.*, 2019, **9**, 5274.

65 M. Back, J. Ueda, H. Nambu, M. Fujita, A. Yamamoto, H. Yoshida, H. Tanaka, M. G. Brik and S. Tanabe, Boltzmann Thermometry in Cr3+-Doped Ga2O3 Polymorphs: The Structure Matters!, *Adv. Opt. Mater.*, 2021, **9**, 2100033.

66 M. Back, J. Ueda, J. Xu, K. Asami, M. G. Brik and S. Tanabe, Effective Ratiometric Luminescent Thermal Sensor by Cr3+-Doped Mullite Bi2Al4O9 with Robust and Reliable Performances, *Adv. Opt. Mater.*, 2020, **8**, 2000124.

67 M. D. Dramićanin, B. Milićević, V. Đorđević, Z. Ristić, J. J. Zhou, D. Milivojević, J. Papan, M. G. Brik, C.-G. Ma, A. M. Srivastava and M. Wu, Li2TiO3:Mn4+ Deep-Red Phosphor for the Lifetime-Based Luminescence Thermometry, *Chemistry Select*, 2019, **4**, 7067–7075.